Internet-Based Image Analysis Quantifies Contractile Behavior of Individual Fibroblasts inside Model Tissue

Steven Vanni,* B. Christoffer Lagerholm,* Carol Otey,† D. Lansing Taylor,* and Frederick Lanni*
*Department of Biological Sciences, Carnegie Mellon University, 4400 Fifth Avenue, Pittsburgh, Pennsylvania 15213; and
†Department of Cell and Molecular Physiology, University of North Carolina, Chapel Hill, North Carolina 27599

ABSTRACT In a cell-populated collagen gel, intrinsic fiber structure visible in differential interference contrast images can provide markers for an in situ strain gauge to quantify cell-gel mechanics, while optical sections of fluorescent protein distribution capture cytoskeletal kinematics. Mechanics quantification can be derived automatically from timelapse differential interference contrast images using a Deformation Quantification and Analysis software package accessible online at http://dqa.web.cmu.edu. In our studies, fibroblast contractile machinery was observed to function entirely within pseudopods, while GFP-alpha-actinin concentrated in pseudopod tips and cortex. Complex strain patterns around individual cells showed instances of both elastic and inelastic strain transmission, suggesting a role in observed long-range alignment of cells.

INTRODUCTION

To extend quantification of single-cell mechanics into three-dimensional (3D) model tissue, we have combined three techniques: 1), growth of fibroblasts within a type I collagen hydrogel; 2), timelapse imaging of cell populations, single cells, and cytoskeletal structure; and 3), quantification of cell-matrix mechanics at the single cell level using the extracellular matrix (ECM) as an in situ strain gauge. A Deformation Quantification and Analysis (DQA) software package (accessible online at http://dqa.web.cmu.edu) was developed to track material deformation as a displacement field without requiring the use of exogenous marker particles. Applied to cells within a collagen gel, it relies only on gel fiber structure to provide pattern information for tracking. This extends single-cell force measurement capability from two-dimensional (2D) substrata to the measurement of strain and stress fields generated in 3D model tissue. Mechanics can then be compared directly to simultaneous observations of cytoskeletal protein localization in individual cells. The comparison aids in the definition and localization of cytoskeletal devices functioning within the cells as they drive the overall system mechanics, and opens the door to studying associated signaling pathways, cell-cell effects, and differentiation in a system more closely related to real tissue.

For over three decades cell biologists have championed model systems which resemble the 3D tissue environment more closely than typical 2D culture substrata (Walpita and Hay, 2002; Elsdale and Bard, 1972; Bell et al., 1979; Tranquillo, 1999; Roy et al., 1999; Grinnell, 2000; Cukierman et al., 2001). Accumulating data highlights differences between 2D and 3D models relating to cell morphology (Walpita and Hay, 2002; Grinnell, 2000), growth and differentiation (Hay, 1993), motility (Walpita and Hay, 2002; Elsdale and Bard, 1972; Tranquillo, 1999; Roy et al., 1999), drug response and antigen presentation (Hoffman, 1993), and the size and composition of cell adhesions (Cukierman et al., 2001). Among the most significant limitations of conventional 2D substrata are their incompliant nature and the restriction of cell adhesions to coplanarity (Roskelley et al., 1994).

Elastic planar substrata restore the compliance found in native tissue and were developed to permit the study of mechanical aspects of cell behavior. Deformable silicone films have allowed cell traction to be visualized as wrinkles in the substratum (Harris et al., 1980) and quantified (Burton et al., 1999). As an alternative to analysis of wrinkle formation, marker particles and micropatterning have been used to quantify traction generated by cells on top of silicone films (Oliver et al., 1995; Balaban et al., 2001), polyacrylamide (PAA) hydrogel substrata bonded to glass (Pelham and Wang, 1999), and collagen gels (Roy et al., 1999; Butler et al., 2002). Motile fibroblasts have been shown to change their direction of travel in response to strain in an underlying PAA substratum (Lo et al., 2000). Such mechanical properties have also been shown to regulate growth and apoptosis (Wang et al., 2000).

A step closer to natural conditions is the study of cells embedded in 3D tissue models, often based on collagen in hydrogel form (Bell et al., 1979). Such studies have included single-cell methods allowing characterization of morphology and intracellular structure (Harkin and Hay, 1996; Voytik-Harbin et al., 2001; Farsi and Aubin, 1984; Cukierman et al., 2001) as well as cell-population methods allowing measurement of aggregate cell-generated forces (Kolodney and Wysolmerski, 1992; Freyman et al., 2002), whole tissue contraction (Grinnell, 2000), and fiber alignment (Tower and Tranquillo, 2001). In some cases, whole gel force measurements have been analyzed to yield average values on a per-cell basis (Kolodney and Wysolmerski, 1992; Brown et al., 1998; Freyman et al., 2001). These methods of quantifying cell contractility have identified proteins and signaling

Submitted June 6, 2002, and accepted for publication October 16, 2002.
Address reprint requests to Frederick Lanni, Carnegie Mellon University, 4400 Fifth Ave., Box 32, Pittsburgh, PA 15213. Tel.: 412-268-3460; E-mail: lanni@cmu.edu.

0006-3495/03/04/2715/13 $2.00

pathways involved in force generation and transmission to the ECM (Parizi et al., 2000; Kolodney and Elson, 1995; Skuta et al., 1999; Cooke et al., 2000; Rosenfeldt and Grinnell, 2000).

In fibroblasts, as in muscle tissue, the cellular forces of contraction and locomotion are generated by the actomyosin cytoskeleton (Grinnell, 1994; Ehrlich et al., 1991). Tractions are coupled to the ECM via collagen-specific integrins, primarily $\alpha 2\beta 1$ (Gullberg et al., 1990; Schiro et al., 1991; Cooke et al., 2000). Alpha-actinin is one of the few proteins known to bind both actin (Lazarides and Burridge, 1975) and integrins, including the $\beta 1$ subunit (Otey et al., 1993). In cells grown on rigid planar substrata, α-actinin is a component of both focal adhesions and actin stress fibers. The present study focused on the intracellular distribution of the major nonmuscle isoform of α-actinin, α-actinin-1, fused to green fluorescent protein (GFP) (Edlund et al., 2001).

In elastic models, mounting the tissue construct is a variable critical to cytoskeletal dynamics and cell behavior (Hay, 1993; Huang et al., 1993; Lin and Grinnell, 1993). Gel configurations can be adherent to a substratum or other support, i.e., anchored, or they can be unanchored (Grinnell, 2000). When anchored, initial constraints may be maintained throughout the experiment or released after cell-driven ''pre-stress'' has developed. Release after pre-stress leads to rapid contraction (within minutes) via a mechanism which likely differs from contraction over hours or days when not using the pre-stress model (Grinnell et al., 1999; Cooke et al., 2000). When no stress is present, fibroblasts do not assemble fibronectin fibrils (Halliday and Tomasek, 1995). The present study used uniaxial isometric mounting which was established immediately upon gel formation and maintained throughout experiments (Huang et al., 1993).

While working in such a system is highly advantageous for biological reasons, a 3D mechanics analysis is difficult because it requires material tracking between planes of focus. However, simplifications can be made that allow a 2D mechanics analysis to capture the key features of the elastic interaction between cell and matrix. This is because it is easy to find elongated cells which can be imaged mostly in one plane of focus and for which out-of-plane material displacements can be ignored. Plane-strain analysis (Fung, 1977) then correctly captures the in-plane deformation of the material surrounding the cell. This is the approach used here with the knowledge that it does not account for a circumferential component of strain.

The elastic 3D nature of this specimen and the long duration of the experiments presented three challenges—optical accessibility, controlled mounting, and specimen viability. The need for precise optical sectioning to image ECM and cytoskeletal structure as well as the short working distance of high numerical aperture (NA) objectives combine to restrict specimen dimensions. To meet these restrictions plus isometric mounting constraints, the design adopted here consisted of a miniaturized, sparsely populated gel (~100 μm between cells) cast in a mesh retainer and mounted within the working distance (~200 μm) of a high-NA water immersion objective. Because experiments spanned hours or days, a recirculating gravity-feed perfusion system was developed to provide long-term cell viability while preserving focus stability (Lagerholm et al., 2003).

Much has been learned about the behavior of fibroblasts growing in a collagen gel. In the presence of 10% serum, cells sparsely embedded in a uniaxially constrained gel migrate moderate distances (~300 μm), show repetitive contractile behavior and proliferate to confluence, leading to contraction of the entire gel (Dickinson et al., 1993). Over 6–12 h, unanchored gel edges retract by 5%. Over 5–7 days, contraction reaches 50% or more (Grinnell, 2000) and is accompanied by syneresis (Bell et al., 1979). Because cells in this type of specimen are often sparsely seeded, we expect that the normal short range biochemical interactions mediated by secretion and binding of growth factors (paracrine interactions) will be attenuated relative to dense cultures. When, during long-term experiments, cells reach near-confluent densities, we would expect the full range of cell-cell interactions to occur. Cells on either surface of the gel are more motile than the embedded cells, with some traveling more than 1000 μm, but these cells exhibit less contractile behavior (Roy et al., 1999). Some motility but no gel contraction is seen under serum-deprived conditions (<2% serum; Nakagawa et al., 1989). Beyond these established observations more information is needed about the detailed mechanical interaction of individual cells with the ECM to better understand the cytoskeleton and the regulation of adhesion and motility in a 3D tissue environment.

METHODS

Cell Culture

Swiss mouse 3T3 fibroblasts expressing either GFP-α-actinin (Edlund et al., 2001) or YFP-β-actin (Lagerholm et al., 2003) were grown in bicarbonate-buffered Dulbecco's modified Eagle's medium (Gibco, Rockville, MD, invitrogen.com) supplemented with 10% calf serum (growth medium, Gibco). During long-term culture, stable transformants were maintained using growth medium with 0.5 mg/mL geneticin (G418, Gibco). To prepare a cell suspension, cells were detached from tissue culture flasks using 0.05% trypsin (Gibco), diluted in growth medium, sedimented in a tabletop centrifuge at 1000 rpm for 7 min and resuspended in phenol red-free growth medium. From this point on, growth medium was always phenol red-free to reduce background during fluorescence microscopy. The cell suspension was briefly stored on ice for use in making cell-populated collagen gels.

Cell-populated collagen gels

Gel solution was mixed from Vitrogen Type I collagen (Cohesion, Palo Alto, CA) following the manufacturer's suggested protocol. In brief, gel solution was prepared on ice by neutralization of Vitrogen 100 stock with 10× PBS (0.2 M Na_2HPO_4, 1.3 M NaCl, pH 7.4) and 0.1 M NaOH in a ratio of 8:1:1. Cell-gel solution was prepared by mixing the above cell suspension into the

gel solution. Volumes were set to produce a final collagen concentration of 2 mg/mL. Gelation was inhibited by storing the mixture on ice.

Cell-populated gels were poured in two equivalent ways. Initially, and for all except the nocodazole/cytochalasin and scanning electron microscopy experiments, two tabs of nylon mesh cut from sheet stock (CMN-350, Small Parts, Miami Lakes, FL, smallparts.com) were glued on one edge to a 40-mm #1 coverslip 5 mm apart (Fisher Scientific, Pittsburgh, PA, fishersci.com). A Teflon square (0.005″ thick, Small Parts) was inserted under the free edges between the two mesh tabs. Approximately 65 μL of the populated gel solution was pipetted onto the Teflon between the mesh tabs to form a 5-mm square gel. The gel solution flowed on top of the Teflon and partly into the mesh, thus anchoring the gel on two ends while not allowing it to adhere to the coverslip below. A later adaptation of this method was used in nocodazole/cytochalasin experiments. Nylon mesh rings were cut from sheet stock (CMN-185, Small Parts) using 0.250″ and 0.375″ hole punches (#402 and #448; M.C. Mieth Mfg., Port Orange, FL, holepunch.com) for the inside and outside diameters (Lagerholm et al., 2003). The rings were placed on Teflon, and 65 μL of the populated gel solution was pipetted into each ring. The gel solution completely wetted the mesh and filled its inner area.

In both cases, gels were made to contain 500–1000 cells. After pipetting, specimens were incubated at 37°C for 60 min in a humidified CO_2 incubator to cause gelation. During gelation, ~15% of the water volume was lost through evaporation, leaving a gel 150–300 μm thick at the center with 20–40 cells/mm^2 projected area. Most of the cells accumulated within the lowest 50 microns of the gel. Immediately afterward, specimens were submerged in growth medium, and the Teflon barrier was gently removed. This defined the initial relaxed state of the uniaxially constrained gel. The gels were then incubated in growth medium at 37°C in 5% CO_2 until use, when they were assembled into a perfusable, temperature-controlled microscopy chamber (FCS2, Bioptechs, Butler, PA, bioptechs.com). For gels cast in mesh rings, two parallel cuts were made in each gel, using a scalpel to leave a 2–3 mm × 6 mm strip of gel anchored at two ends but free on two sides as well as on top and on bottom.

Nocodazole and cytochalasin D treatments

Cell-populated collagen gels were prepared, incubated overnight, and then cut as described above. During these experiments, gels were bathed in bicarbonate buffered phenol red-free glutamine-deficient Ham's F-12 medium (9589, Irvine Scientific, Santa Ana, CA, irvinesci.com) containing 10% calf serum and 25 mM HEPES (pH 7.3) for additional pH control under ambient conditions. Unperturbed cell-gel behavior was recorded for a minimum of 30 min before drug perfusion, and timelapse imaging then ran continuously throughout each experiment. Approximately 10 ml of 25 μM nocodazole (R17934, BIOMOL Research Labs., Plymouth Meeting, PA, biomol.com) in the same medium was gravity-fed into the specimen chamber, displacing the initial medium. 60–90 min later, ~10 ml of 25 μM cytochalasin D (C8273, Sigma-Aldrich, St. Louis, MO, sigmaaldrich.com) was similarly perfused.

Electron microscopy

Cell-populated collagen gels were prepared as described above and incubated 24 h to permit cell spreading but little growth. Gels were then washed 3× in phosphate buffered saline solution (PBS, pH 7.4), fixed for 15 min in 4% EM grade paraformaldehyde in PBS (Electron Microscope Sciences, Ft. Washington, PA, emsdiasum.com) and then washed three times in PBS. Gels were postfixed for 30 min in 1% OsO_4 in PBS, then washed in three changes of dH_2O. This was followed by dehydration in an ethanol series (50%, 70%, 80%, 90%, and three changes of 100%). Dehydrated gels were critical-point-dried from liquid CO_2 at 1200 psi and 42°C (CPD2 Dryer, Ted Pella, Redding, CA, pelcoint.com). The dried gel was mounted on a specimen stub, sputter-coated with gold, and viewed by scanning electron microscopy (2460N, Hitachi Scientific Instruments, Mountain View, CA).

Automated timelapse multimode microscopy

Image data was obtained using an automated interactive microscope platform (AIM) (Taylor et al., 1996). AIM combined an inverted microscope (Axiovert 135TV, Zeiss, Thornwood, NY, www.zeiss.com), a motorized x-y stage and piezoelectric focus control. For optical sectioning fluorescence microscopy, the microscope was equipped with a piezo-controlled grating imager (Lagerholm et al., 2003; Lanni and Wilson, 2000). Both high-resolution fluorescence and differential interference contrast (DIC) images were captured using a 40×, 1.2 NA indirect water immersion objective (C-Apochromat, Zeiss) and a cooled CCD camera (Hamamatsu, Bridgewater, NJ, www.hamamatsu.com). The microscope, including the accessories and camera, were controlled via a PC. This computer received user input from, and returned data to, a Unix computer (Onyx, Silicon Graphics, Mountain View, CA, sgi.com) which supported the user interface and data storage. The AIM software interface facilitated a complex timelapse schedule, including assignment of imaging mode and timing to logged stage positions, and permitted modification to this schedule as experiments progressed. A serial-focus image stack was acquired at each DIC time point and less frequently in fluorescence.

During timelapse experiments longer than 4 h and up to several days, culture conditions were maintained using growth medium in a 10 ml 5% CO_2 equilibrated recirculating gravity-feed perfusion system (Lagerholm et al., 2003) flowing at 3 ml/h. This low-volume/slow-flow design maintained cell conditioning of the culture medium and permitted efficient gas exchange. Gravity feed additionally overcomes the pulsation problems of pump-only systems which interfere with focus stability.

DQA deformation quantification module

DQA software is divided into two modules—the first for material tracking and the second for mechanics analysis. In the Tracking module (Fig. 1), deformation is quantified as a field of material displacement measurements $\boldsymbol{U}(x,y) = \{U_x(x,y), U_y(x,y)\}$. This field is determined on a square grid, one location at a time, by comparison of multiple subregions between two images from a time series. The overall displacement field is developed by tracking the x-y shift occurring at individual grid points throughout the image. Square subregions define source and target patterns for matching between images at two time points (Image 1 and Image 2). Pattern size and the spacing between patterns are user-specified parameters. Thus, depending on the user input, adjacent patterns may overlap, exactly abut each other or more sparsely sample the totality of pixels within the overall image.

Tracking at individual grid points works as follows. A search is conducted to locate the best match for the source pattern in Image 1 among the set of target patterns in Image 2 (Fig. 2 *A*). Rather than searching all of Image 2, a neighborhood around the original grid location is defined as the search area. The search area is a square centered on the source pattern and has a user specified half-width defined as the ''search radius''. The search area defines a small set of target patterns, one centered on each pixel in the search area. As the search area is tested, candidate targets are compared to the source by computing the normalized correlation coefficient between source and each target (Fig. 2 *B*). The location of the target pattern producing the largest correlation coefficient determines the integer x-y displacement at that grid point. A 2D parabolic fit around this maximum in the correlation coefficient array then provides an approximate fractional-pixel refinement (Fig. 2 *C*).

Because the goal is to track material displacement, two steps are taken to eliminate erroneous vectors. First, intracellular events such as organelle transport may or may not be mechanically related to deformation of the gel matrix, so a masking feature is provided. The user submits a binary image (a mask) with zero valued pixels used to indicate portions of the image which are not to be tracked. Masks are typically derived either from a manual tracing of the cell(s) in a DIC image or from a thresholded fluorescence image. Second, an attempt is made to filter out displacement vectors which do not vary smoothly on a spatial scale set by the user. For example, spurious

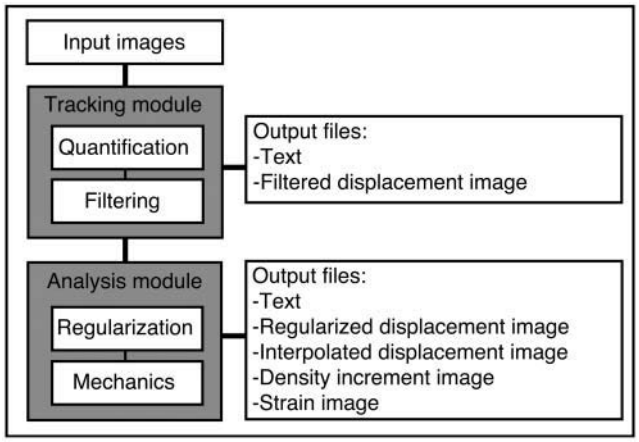

FIGURE 1 Flowchart of DQA processing (see Methods).

vectors would result from tracking free-moving particles or portions of cells which are not masked. To implement filtering, tracking is repeated at four or eight locations neighboring a given grid point at a specified distance, and the average and standard deviation of the resulting set of displacement vectors is computed. A user-supplied threshold determines the acceptable standard deviation of the set and operationally defines spurious tracking. When this occurs, no vector is reported at that grid point and no attempts are made to track there during later time points. Otherwise, the average is reported out as the displacement (U_x, U_y). Tracking may be continued through a timelapse series to obtain both incremental and cumulative displacements.

DQA mechanics analysis module

In the Analysis module (Fig. 1), filtered displacement vectors received from the Tracking module are regularized and interpolated to define the continuous vector field ($U_x(x,y)$, $U_y(x,y)$). This is done independently for the x- and y-displacements by fitting a weighted sum of basis functions to each 2D scalar field ($U_x(x,y)$ and $U_y(x,y)$) by means of singular value decomposition (SVD) (Press et al., 1992). SVD as currently implemented in DQA uses a basis set composed of elementary point-load displacements centered on an assigned subset of boundary points (x_i,y_i) in the mask. The elementary basis function is the 2D vector-valued Cerruti displacement field $\boldsymbol{C}(x,y,0)$ (Westergaard, 1952) convolved with a 2D distributed tangent load. A Gaussian distribution of the load, $(\alpha^2/\pi)\exp(-\alpha^2 r^2)$, suppresses divergence at the load point. Each Cerruti-Gauss basis function, $\boldsymbol{CG}(x\text{-}x_i,y\text{-}y_i,0)$, is utilized in 2 × 2 tensor form to represent displacements caused by any combination of normal and tangent tractions at the cell boundary within the image plane. This basis set outperformed a standard Fourier basis set.

After regularization, three displacement fields are returned as output files: 1), the tracker displacement data with vectors missing where tracking failed, 2), regularized displacements at all points where tracking was successful, and 3), a regularized, interpolated displacement field where a vector is calculated at all grid points outside of the mask (Fig. 6 *A*). Locations where tracking failed are assigned interpolated vectors from the SVD solution.

After regularization, three mechanics analyses are performed on the displacement data: 1), 2D density increment; 2), plane strain; and 3), Hookean plane stress.

1. A normalized 2D density increment $\Delta d(x,y)/d_0$ is calculated from the regularized interpolated displacement field wherever four grid points originally adjacent in a square exist outside the mask. Density as defined here is inversely proportional to the area between the four grid points, $d \sim 1/A$ and $\Delta d = (1/A) - (1/A_0)$. The density increment is calculated as the fraction $\Delta d/d_0 = (A_0 - A)/A$. This measure is positive for compaction of the quadrilateral and negative for expansion. It is scaled and mapped to a blue-red color scale, and the color is then assigned to that quadrilateral in the displaced image. Compaction is assigned to the red side of the spectrum; zero density change is purple; and expansion is assigned to blue (Fig. 6 *B*).
2. Plane strain is calculated at each grid location from Cartesian derivatives of the SVD fitted field. In the plane-strain approximation (Fung, 1977), strain is a 2 × 2 tensor: $e_{ij} = (\partial U_i/\partial x_j + \partial U_j/\partial x_i)/2$. The value of the tensor field at each grid point is displayed as principal strains in a ''strain

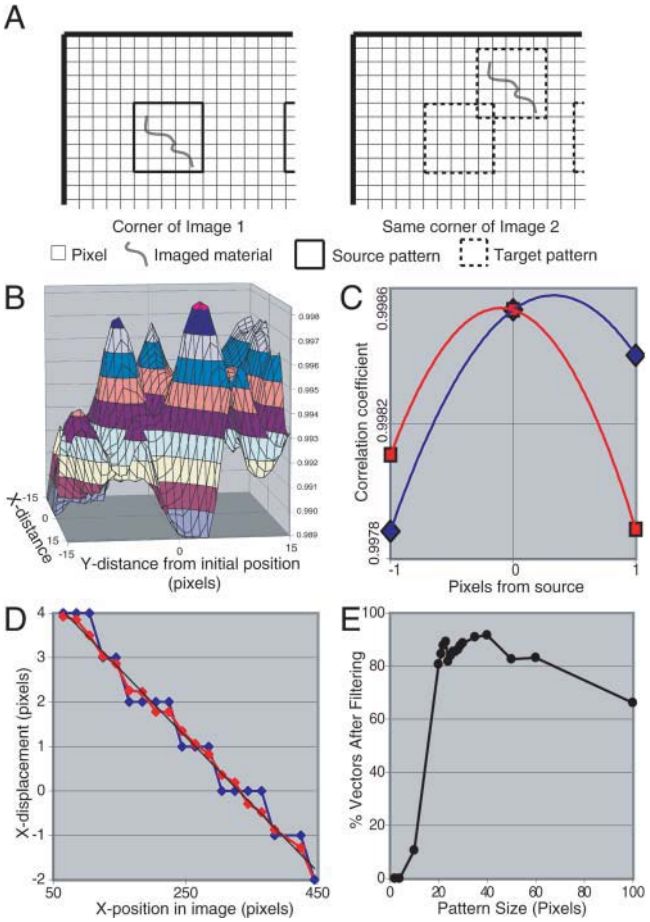

FIGURE 2 DQA Tracker operation. (*A*) Schematic of pattern matching. Around each grid point, all of the target patterns together constitute the search area, though for clarity only two target patterns are shown here. (*B*) Plot of correlation coefficients over one search area in processing images of a collagen gel specimen. (*C*) Parabolic fit of correlation coefficients to find the fractional interpolation for $\boldsymbol{U}(x,y)$ at one grid point. Shown are parabolas fit to the maximum correlation coefficient and its immediate neighbors for both U_x (*blue*) and U_y (*red*) to interpolate a vector offset. The location of the maximum on each parabola provides a fractional pixel correction to the integer displacement measurement. (*D*) Demonstration of improved accuracy resulting from interpolation. DQA was used to compare the image of a collagen gel to a rotated version of this same image. Rotating the image 10° caused the x-component of displacement to vary linearly across the image (*black*). Because the tracker generates target patterns located at integer shifts from the initial position, intermediate tracker values are integers, resulting in artifactual stair-step offsets (shown here in *blue*, although not normally output). A fractional pixel interpolation (*red*) reduces this artifact. These fractional values are then filtered and output. (*E*) Effect of pattern size on tracking success for typical cell-driven deformation in collagen.

cross''. The principal strains are derived by computing the eigenvalues (λ_1,λ_2) and orthonormal eigenvectors ($\mathbf{v}_1$,$\mathbf{v}_2$) of [e_{ij}] at each grid point and scaling each eigenvector by the corresponding eigenvalue ($\lambda_1\mathbf{v}_1$,$\lambda_2\mathbf{v}_2$). Positive principal strains, which represent extension, are coded blue, and negative strains, representing compression, are coded red (Fig. 6 *C*). As defined, density increment is related to the principal strains by $\Delta d/d_0 = -(\lambda_1 + \lambda_2)$.

3. Under small displacements, the collagen gel should behave like a Hookean solid. In this case, a simple relation exists between strain and stress: $[\sigma_{ij}] = \Lambda(\text{trace}[e_{ij}])[I] + 2G[e_{ij}]$. This relationship is characterized by the elastic modulus (G) and Poisson's ratio for the material (ν), both of which determine the Lamé coefficient $\Lambda(G,\nu)$. When these values are known, the stress field can be derived from the strain field.

The mechanics model incorporates two simplifications: 1), analysis is based on the plane-strain approximation; and 2), analysis takes as input measurements from a single plane of focus. Sufficiently sharp depth of field is required so that optical sectioning defines planes where displacement can be determined unambiguously. Because of the thin, uniaxial specimen mounting system, cells tended to align horizontally in the gel, making it possible to select a single image plane containing the cell axis. The approximate axisymmetry defined by cell orientation and optical sectioning allowed quantification of axial and radial components of strain but not circumferential components.

Testing of the deformation quantification module

For DQA tracker testing, image sets containing uniform displacement fields of known magnitude were generated either by image processing or by controlled movement of the microscope stage. These DIC images (not shown) were of cell-free collagen gels unless otherwise indicated. Essentially noise-free image pairs were generated by shifting a single image by a whole or fractional number of pixels using Adobe Photoshop (Adobe Systems Incorporated, San Jose, California, www.adobe.com). Half-pixel shifts were achieved by first increasing the image pixel count fourfold using pixel duplication, shifting the image one pixel along one axis, and then decreasing the pixel count fourfold using nearest neighbor averaging. The images in this pair had identical noise content except for insignificant processing error. Image pairs with significantly differing noise content were generated by acquiring two images in rapid sequence with or without intervening movement of the motorized stage.

Traction simulation

Tractions were modeled as discrete loads applied over a Gaussian footprint tangent to the surface of an elastic half-space. A modification of the Cerruti equations was used in a method analogous to that used in the basis sets for DQA regularization (Analysis module). The simulation computed the 2D surface displacements, ignoring any z-component, with a Gaussian width of 50 pixels and 0.23 for Poisson's ratio.

RESULTS

Deformation quantification and analysis

DQA takes two or more timelapse images as input to a tracking module which uses pattern matching to determine material displacement at multiple grid locations and then filters out spurious matches. Filtered displacements feed into an Analysis module, which regularizes the data to generate a smooth deformation field and carries out a mechanics analysis (Fig. 1).

Several aspects of DQA facilitate analysis of complex displacement fields over time. First, repetitive and subjective human interactions are minimized. No particles need be identified for tracking, but a masked area may be specified where tracking will not be attempted (see Methods). Multiple time points are processed without user intervention. Second, typical image pair processing can be accomplished in 15 s to 2 min on a personal computer. Finally, anyone may use this software package directly on the Internet (http://dqa.web.cmu.edu).

Tracker performance

DQA tracking involves matching each source pattern from an initial time point (*Image 1*) to the most similar target pattern from a subsequent time point (*Image 2*; Fig. 2 *A*). The quality of match is gauged by the magnitude of the correlation coefficients computed between source and target patterns. At each grid location, the maximum correlation coefficient identifies the local 2D material displacement vector $\boldsymbol{U}(x,y) = \{U_x(x,y),U_y(x,y)\}$.

For verification, three aspects of tracker performance were examined: 1), behavior of the correlation function; 2), interpolation of integer measurements of displacement to gain subpixel accuracy; and 3), experimental evaluation of the overall accuracy. Correlation coefficients showed multiple local extrema with a global maximum (Fig. 2 *B*), and success in tracking generally relies on the presence of such a maximum at the correct x-y location within each search area.

Because actual material displacements rarely coincide with integer pixel units, interpolation yields a better measure of displacement $\boldsymbol{U}(x,y)$. Inspection of correlation coefficients surrounding the maximum generally showed monotonic decrease from which a fractional-pixel refinement could easily be interpolated (Fig. 2, *B* and *C*). Increased smoothness in $\boldsymbol{U}(x,y)$ due to interpolation was demonstrated in processing a data set containing a known displacement field (Fig. 2 *D*). Interpolation generally improved both density increment and strain analyses (see Methods).

Trial runs helped to optimize the three user-specified parameters which enter into the tracking process—pattern size, distance to neighbor for sparse filtering, and filtering threshold. Optimization was accomplished by maximizing the percentage of grid points which survive filtering. The percentage plateaued for pattern sizes between 20 and 40 pixels (Fig. 2 *E*). This was expected because a small source pattern may match more than one target by failing to capture enough spatial information in the local material. On the other hand, large patterns average over and therefore fail to detect local deformations. Inasmuch as computation time increases as the 4th power of pattern size, the lower end of the plateau (20 pixels) was the most desirable operating point. In filtering, as distance to neighbor increased and threshold

decreased, the percentage predictably declined (data not shown). Understanding the best parameter values under these trial conditions provided a starting point for further optimization during actual processing.

Tracking accuracy was on the order of 0.5 pixel, based on three tests. The first test used a single image which was then computationally shifted to produce a noise-free image pair with a known uniform displacement between the two images. In this case, the standard deviation of the error values after tracking averaged 0.01 pixel. Thus, gel structure allowed for very accurate tracking when there was little noise in the data. The second test used two images of gels without cells. The images were acquired in rapid sequence with no movement of the specimen. In this case ideally measured displacement values would be nearly zero everywhere. In practice this yielded the smallest scatter for real data, with a standard deviation of 0.37 pixel. The final test was similar to the second except that the microscope stage was moved transversely between acquisitions. In this case scatter increased to 0.50 pixel and was only weakly dependent on the size of the movement. Processing this same data with tighter filter parameters improved accuracy but reduced the number of data points that survived filtering.

Simulation of cell-gel mechanics

To help interpret biological data including coarse inference of the traction locations giving rise to observed gel displacements, simple traction combinations applied to an elastic continuum were simulated, and the resulting displacement data was processed using just the DQA Analysis module (see Methods). A single tangent load demonstrated key features of density increment and strain: trailing material extension, leading compression, and adjacent shear (Fig. 3, *A–C*). To aid in modeling cell-driven contraction, a contractile unit was generally defined as a set of applied loads which sum to zero and produce zero net torque. A simple case with a pair of well-separated contractile loads resulted in a ''double peak'' compression pattern in the density plot (Fig. 3, *D* and *E*). Principal strain analysis showed regions where tangent traction was or was not applied (Fig. 3 *F*).

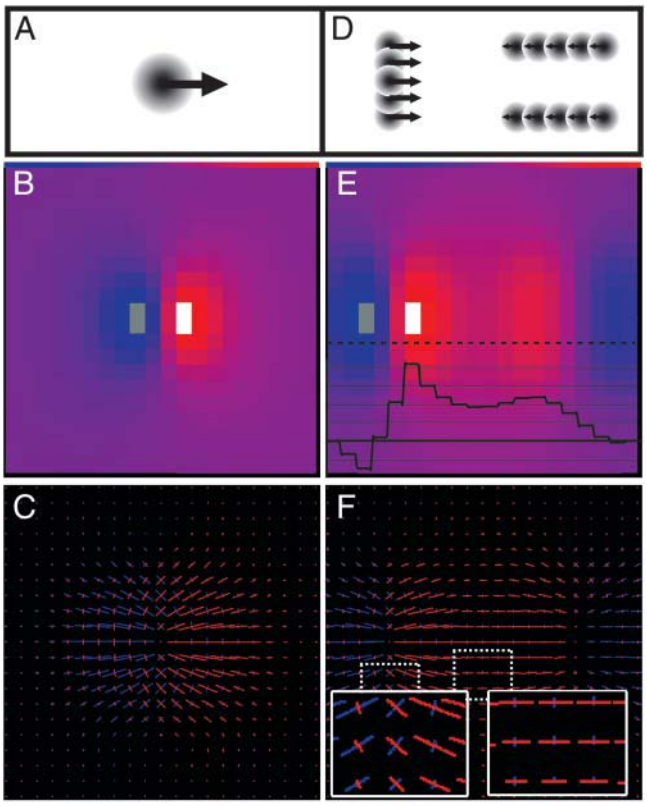

FIGURE 3 Simulated effects of tractions applied tangent to the surface of an elastic gel. (*A*) Single applied load pulling to the right. Shading shows 2D Gaussian load distribution. (*B*) 2D density increment resulting from *A*. Extension trails the load (*blue*; peak in *gray*), whereas compression leads the load (*red*; peak in *white*). (*C*) Principal strains resulting from *A* shown as strain crosses (see Methods). Shear strain appears lateral to the load and is identifiable where strain cross orientation is 45° to the direction of traction. This may be compared to nearly pure extension and compression (*left* and *right* of the load) where one principal component of strain is collinear with the traction. (*D*) Contractile unit (zero net traction, zero net torque) representing a simple rectangular cell applying a statically balanced set of discrete loads between a leading edge on the left and the two sides of a cell body on the right. Shaded circles show 2D Gaussian load distributions. Each of the five loads on the leading edge was of magnitude +1, whereas each of the 10 loads lateral to the cell was of magnitude −1/2. (*E*) 2D density increment resulting from *D*. Distinct groups of opposed forces within the contractile unit produce interior regions of compression (*red*) and exterior regions of extension (*blue*) which define the ends of the unit. Profile near axis shows typical compression double peak (*dotted line* and *inset*). (*F*) Strain crosses resulting from *D* showing shear lateral to the tractions (*left inset*) and nearly pure compression between the tractions (*right inset*).

Cell-gel behavior

In typical experiments, multiple locations in the gel were imaged over periods ranging from 4–60 h during which cells produced large-scale changes in the overall dimensions of the gel including reductions in width of 50–80% along the unconstrained gel axis. This observation was consistent with previous reports in similar systems (Bell et al., 1979; Grinnell et al., 1999). Whole gel contraction, caused by the aggregate cell population, led to large-scale movement of cells and gel together. During single cell imaging, whole gel contraction contributed a global shift to the locally generated deformation field, but the global contribution was relatively uniform over the small field of view at 40× magnification. This global shift appeared in displacement measurements but did not affect density increment or strain, which are computed from differences and derivatives, respectively.

Typical single cell behavior alternated between pseudopod extension and contraction with intermittent coupling to cell body translocation (Fig. 4 *A*). Cells also exhibited periods of relaxation including pseudopod de-adhesion and retraction. This behavior was consistent with early reports on

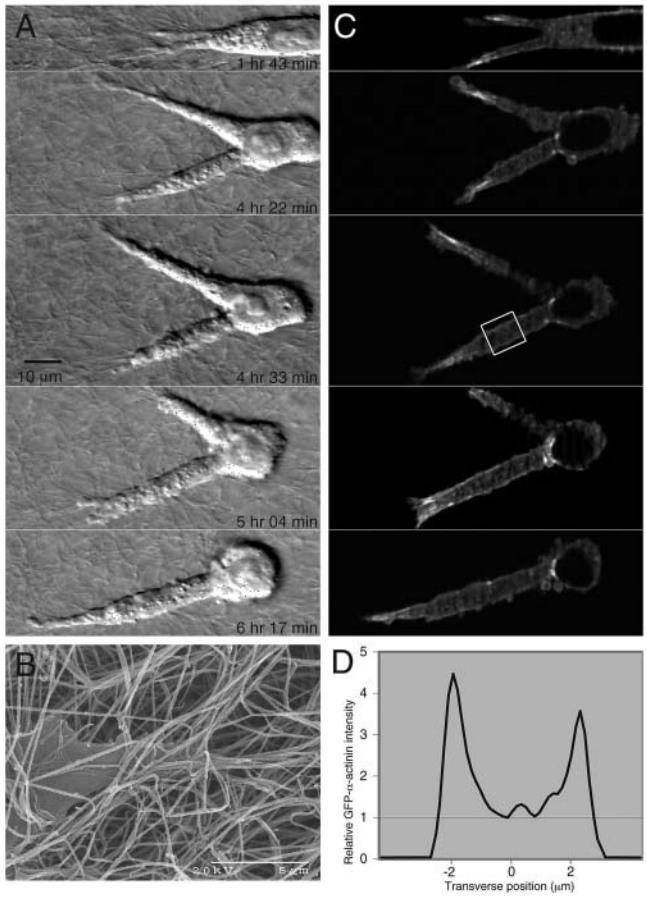

FIGURE 4 Behavior and cytoskeletal structure of individual fibroblasts in collagen gel. Serial-focus image stacks at each time point show the cell was completely embedded ~50 μm above the lower gel surface (data not shown). (*A*) Cell shows typical morphology dominated by large pseudopods. Although the cell moved a relatively small distance, it showed considerable activity, extending two pseudopods, one of which was later retracted as the cell body followed the remaining pseudopod. (*B*) Scanning electron micrograph showing a pseudopod tip in collagen gel. (*C*) GFP-α-actinin fluorescence optical sections approximately matching DIC time points. (*D*) Line profile showing GFP-α-actinin localization to the cortex. Profile is average of fluorescence across box in *C* and shows concentrations of GFP-α-actinin up to four times greater in the cortex than in the endoplasm.

cells in collagen (Elsdale and Bard, 1972). Scanning electron micrographs of cell pseudopods near the gel surface reveal voids within the gel matrix as large as the pseudopod tips but smaller than typical cell bodies (Fig. 4 *B*) and support the idea that cells can extend pseudopods with little gel displacement, consistent with timelapse observations.

Fibroblasts in collagen did not develop stress fibers identifiable via GFP-α-actinin or YFP-β-actin until later in the gel contraction process than the 1–2 days in these timelapse experiments (not shown). This is consistent with reports that ''3D-matrix adhesions'' take several days to develop in 3D tissue models (Cukierman et al., 2001). Instead, GFP-α-actinin, normally a component of actin stress fibers, was seen to concentrate in the cortex and at the distal tips of pseudopods with diffuse distribution elsewhere in the endoplasm (Fig. 4 *C*). Fluorescence profiles from optical sections showed concentrations fourfold greater at the cortex and fivefold greater at the pseudopod tips compared to the endoplasm (Fig. 4 *D*). This was consistent with cortical and ''front end'' distributions of actin reported for fibroblasts in collagen (Walpita and Hay, 2002). YFP-β-actin (not shown) localized similarly to GFP-α-actinin.

The opposing effects of nocodazole and cytochalasin D demonstrated the elasticity of gel deformation caused by short-term, single-cell contractility. These pharmacological agents depolymerize microtubules and actin respectively (Kolodney and Wysolmerski, 1992; Kolodney and Elson, 1995). In the case of nocodazole, rapid gel contraction was observed upon perfusion into a specimen (Fig. 5, *A* and *B*). An opposite but equally dramatic relaxation was observed when cytochalasin D was subsequently perfused into the same specimen (Fig. 5, *B* and *C*). Cumulative DQA processing of multiple timelapse images readily quantified the contraction and showed nearly reciprocal relaxation (Fig. 5, *D–I*).

Pseudopods can behave as discrete contractile devices. During single-cell contraction cycles, density increment and strain were maximal bordering pseudopods with values up to 20% (Fig. 6, *A–C*). Consistent with simulations, line profiles of density increment showed the double-peak pattern associated with a contractile unit (Figs. 6 *D* and 3 *E*). Also consistent with simulations, strain crosses suggested a lack of traction alongside pseudopods with clear indications of traction at pseudopod bases and more complicated patterns at pseudopod tips (Fig. 6 *C*). This indicated that contractile machinery can operate primarily within pseudopods.

Analysis of strain transmission away from the pseudopod tip into the ECM suggested that the ECM does not always respond homogeneously. Simulation predicted a smooth rolloff from compression to extension, but the actual pattern was more complicated with minor compressive zones found distal to the pseudopod tips (Figs. 3 *E* and 6 *B*). A possible explanation is that cells selectively adhere to relatively stiff ECM fibers which then inelastically and more effectively transmit load to distant matrix regions. DQA processing of tiled timelapse image sequences showed strain extending, elastically or inelastically, to distances as great as 800 μm (not shown). The strain effects observed here at the single-cell level are analogous to long-range ''two centre effects'' involving collagen fiber alignment through collective cellular action over distances spanning as much as 4 cm (Stopak and Harris, 1982). Initially isolated cells were observed to divide and mechanically interact with the ECM while repositioning themselves into aligned chains of daughter cells (Fig. 7), a behavior that has been noted previously (Elsdale and Bard, 1972). The strain effects quantified here likely play a role in organizing this type of cell-cell interaction.

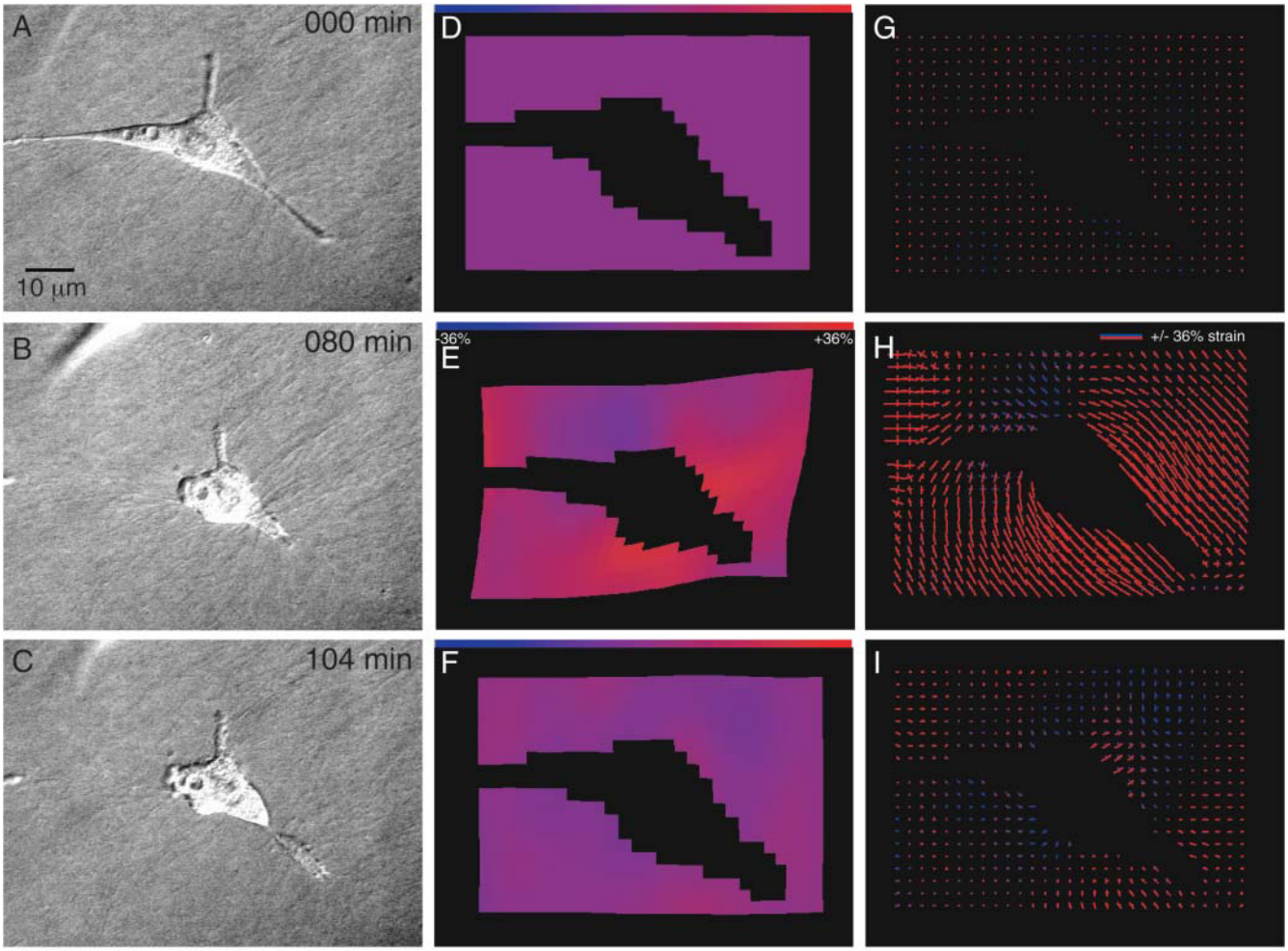

FIGURE 5 Elasticity of cell-driven gel contraction. Specimen was perfused with nocodazole at 001 min and cytochalasin D at 081 min. DIC images were acquired every min. To compute cumulative deformation (first, through nocodazole treatment and then through both treatments), DQA processing was run from 000–080 and from 000–104 using 20 equispaced images in each case. (*A–C*) DIC. (*D–F*) 2D density increment. (*G–I*) Plane strain.

DISCUSSION

Deformation quantification and analysis

The transparency and compact geometry of the collagen model system employed here support acquisition of high-quality DIC images. When combined with use of a high-NA water immersion objective, with its low aberration and high 3D resolution, the pattern information captured is detailed and consistent between time points and thus highly suitable for DQA processing. Several optical factors can degrade image quality, but most are easily controlled. These include focus drift between time points, changes in illumination intensity, random motion of features not linked to the gel (e.g., Brownian motion of particles between gel fibers), and variation in the image background. These factors reduce the useful information content in the gel patterns being tracked, degrading the definition of the correlation coefficient maxima (Fig. 2 *B*), and heightening the likelihood of ambiguous tracking. In general, DQA processing was sufficiently robust to work under typical experimental conditions.

DQA provides a useful tool for rapidly quantifying material deformation and, in particular, gel deformation resulting from cell-applied forces. Given the inhomogeneities in gel structure at the size scale in question, the filtering, averaging, and regularization incorporated in DQA helped greatly in detecting trends within noisy raw displacement measurements (Schwarz et al., 2002). Shifts in the field of view directly affected displacement output, but density increment and strain, being differential quantities, were unaffected.

Spatial and temporal resolution affect tracker performance through the conditions chosen for an experiment and the parameters set during DQA processing. First, there must be sufficient spatial resolution to define the deformations of interest uniquely. Overly similar features in the material can foil the requirement that there be a unique maximum among the correlation coefficients within each search area. Second,

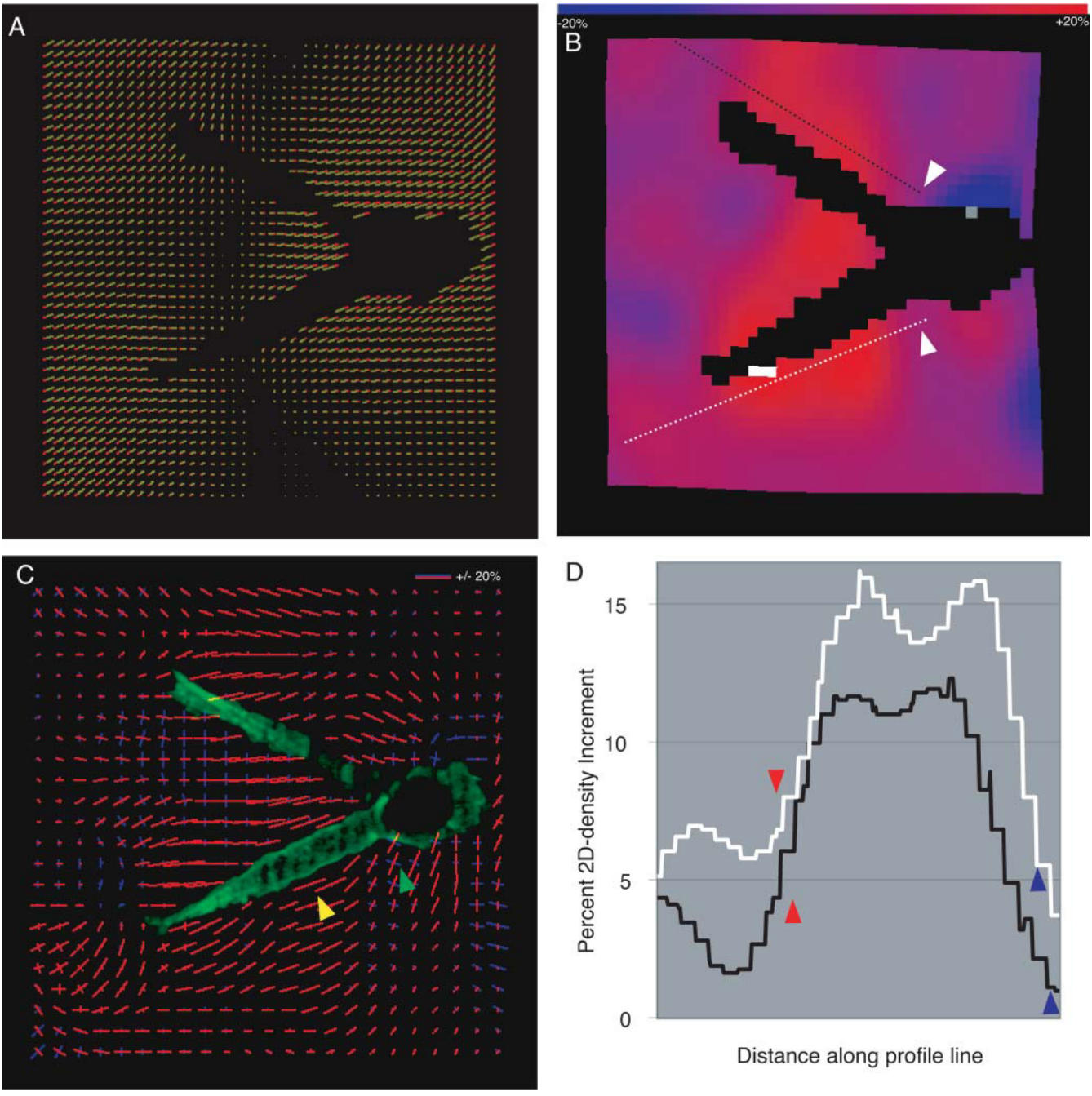

FIGURE 6 DQA analysis of pseudopod contraction. (*A*) Displacement field caused by fibroblast in Fig. 4 *A* between frames 4 h 22 min and 4 h 33 min. A mask suppressed DQA processing within the cell silhouette (see Methods). Vectors (*green*) show displacement from each initial grid point (*red*). (*B*) 2D-density increment resulting from *A*. Compression zones were localized adjacent to the pseudopods, diminishing to neutral density increment with a clear demarcation at the cell body-pseudopod boundaries (*white arrowheads*). (*C*) Principal strains resulting from *A* shown as strain crosses superimposed on corresponding GFP-α-actinin fluorescence optical section. Strain crosses indicate shear and tangent traction close to the pseudopod-cell body boundary (*green arrowhead*), whereas strain crosses indicate absence of shear and compressive strain along the pseudopod axis (*yellow arrowhead*) as explained in Fig. 3. (*D*) Profiles of density increment along the dotted lines shown in *B*. The endpoints of the white and black line scans in *B* correspond exactly to the endpoints of the white and black curves, respectively. Because the line scans are not of the same length, they were individually and linearly scaled to the horizontal axis in *D*. Both leading edge and cell body boundaries occur where the density-increment profiles roll off steeply to values of 6% or less (*red arrowheads* and *blue arrowheads*, respectively, in *D*; reddish-purple density in *B*). Double peak compression patterns are apparent as described in Fig. 3 *E*.

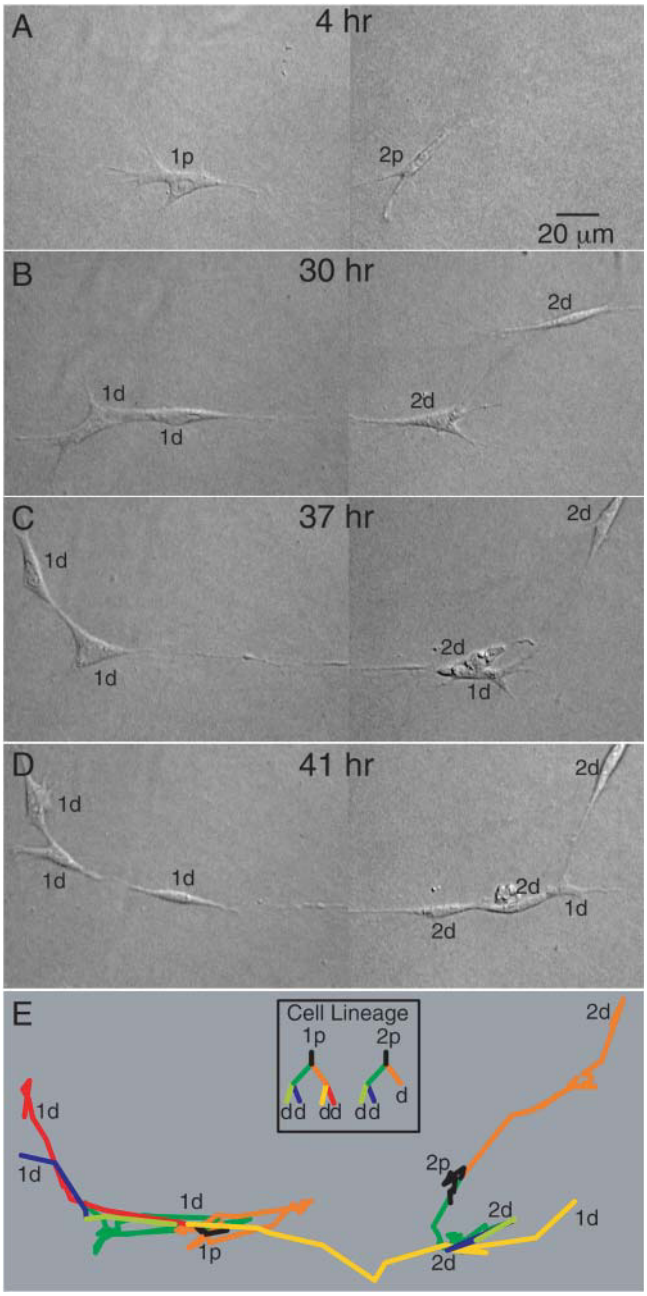

FIGURE 7 Chain formation through cell growth and migration over 37 h. Parent cells *1p* and *2p* in *A* migrate and divide into daughter cells *1d* and *2d* as shown in *A–D*. In *E*, cell tracks are traced over the entire time period with coloring to indicate cell lineage. Paths are corrected for gel movement. Labels are shown for initial and final cell positions.

the target pattern which is to match the source pattern must have remained sufficiently similar to the source pattern through the deformation occurring over the timelapse interval. With DQA statistical filtering, tracking failure becomes apparent as a loss of output displacement values. This is because typical error sources show up as increased scatter in the data. Statistical quantification of this scatter provides a useful indication that a problem is occurring. Similarly, tightened filtering improves accuracy, while reducing the percentage of recovered grid points. To a limited extent, loss of data can be overcome by increasing the number of grid points (with a linear increase in processing time). Alternatively, the percentage of grid points surviving filtering can be increased by changing other processing parameters or, if necessary, experimental conditions such as magnification, camera pixel size, timelapse interval, or gelation conditions (as they affect matrix structure).

The relative ease with which timelapse images can be processed suggests that other materials may also be imaged and tracked, including 2D substrata (e.g., silicone membrane or polyacrylamide gel) and materials used in tissue engineering (e.g., fibrin gel). The basic condition is simply that the material presents high transparency and sufficiently high-contrast pattern information. Because others may find DQA useful in studying similar or different material systems undergoing deformation, this software has been made available for use directly via the Internet. First-time visitors can learn the capabilities of the software in a tutorial area of the website. After requesting a password, users can explore capabilities using images provided for practice runs or may proceed directly to processing their own images which will be uploaded and processed with results returned in real time. A future version of DQA software could be downloadable as a plug-in or stand-alone executable.

Cell-gel behavior

These results show that a collagen-based model ECM can be used as an in situ strain gauge without exogenous marker particles. Mechanics analysis reveals the effects of cellular contractile mechanisms and allows these effects to be compared with simultaneous localization of cytoskeletal components. The data and analysis are more than sufficient for addressing motile mechanisms on the size range of interest—from regions of single cells up to distances spanning the entire gel and events between separated cells.

Fibroblasts in collagen rapidly develop relatively long pseudopods showing cortical concentration of GFP-α-actinin and YFP-β-actin which culminates in dense localization throughout the pseudopod tips. The distal concentration may be analogous to the cortical concentrations seen midway along the pseudopod, differing only in that the endoplasmic volume in the tips is relatively small, creating a high concentration in the tip. This agrees with previous reports on cortical actin (Cukierman et al., 2001; Walpita and Hay, 2002) and is in contrast to the lamellipods, punctate focal adhesions, and stress fibers seen in fibroblasts on planar substrata. It remains to be seen whether the concentrations of GFP-α-actinin seen here (Fig. 4 *C*) are related to the rapid (60 min) coalescence of GFP-α-actinin at nascent focal adhesions on glass (Edlund et al., 2001; Cukierman et al., 2001). Whereas fibroblasts in the experiments reported here did not develop stress fibers, contact formation and force

application were seen to occur through the cell's mechanical effects on the gel. Because cells in early-stage gels are devoid of stress fibers, it is likely that the cortical cytoskeleton constitutes the major portion of the contractile unit machinery.

Cells in collagen see a complex presentation of molecular and physical features with a third dimension added to the surface composition and topology of planar substrata. This is in large part due to the structure of materials like glass, rubber, and PAA which are chemically and mechanically homogeneous down to a much smaller spatial scale than collagen and cannot be invaded by fibroblasts. Thus, it may not be surprising that, if a 2D surface supports adhesion, then focal adhesions tend to be well formed and numerous (Pelham and Wang, 1999; Balaban et al., 2001; Edlund et al., 2001; Cukierman et al., 2001). In contrast, migration through a gel is less like crawling on a carpet and more like climbing through tree tops. On planar substrata a cell is free to move in any direction, and, even after commitment to one direction, the substratum does not mechanically prevent a change. A cell can simply swerve. A cell navigating a collagen meshwork, however, is subject to impediments similar to that seen in polymer reptation (e.g., migration of DNA strands in agarose electrophoresis). In this case, changing the path of travel requires retraction from one penetration into the meshwork and commitment to a new path (Fig. 4). As shown, cells in collagen extend processes to probe their surrounding meshwork for considerable distances (10–100 μm) before pseudopod stabilization and mechanical interaction. To eventually translocate, cells must navigate the meshwork, the porosity of which can be smaller than the largest cell dimensions (Tranquillo, 1999). Thus the cells must either alter their shape or remodel the meshwork through deformation or degradation. In contrast to fibrin gels (Mirshahi et al., 1991), fibroblasts do not appear to significantly degrade collagen gels (Guidry and Grinnell, 1985). Because of this 3D complexity, contact formation may involve micron-scale mechanical interactions in addition to molecular binding.

Deformations caused by isolated cells over short time periods (minutes) appear to be reversible in the cell-gel specimens studied here. This is emphasized by rapid manipulation of cell contraction through the use of nocodazole and cytochalasin D. Over longer periods of time, release of cell generated forces through cytochalasin D treatment leads to only partial reversal of whole-gel contraction (Guidry and Grinnell, 1985). This may result from a ''locking-in'' of compaction which occurs over time due to enzymatic cross-linking of collagen gel fibrils (Siegel et al., 1982).

Although we did not carry out a detailed force analysis, it is possible to estimate pseudopod traction forces from DQA strain fields. In these experiments, maximum gel strain near the pseudopod center ranged as high as 20% in single contractile cycles. If the pseudopod is simply modeled as a pair of opposed, Gaussian-distributed loads, compressive strain at the midpoint (ε_x) is relatively uniform and proportional to load force, $F_x = (15{,}700)G(L_0)^2\varepsilon_x$ (nN), where L_0 is pseudopod length (cm) and G is gel modulus (dyn/cm^2). For a 60-μm pseudopod and gel modulus of 55 Pa (Velegol and Lanni, 2001), the computed contractile load is 60 nN. This is a very small load compared to observations with fibroblasts on 2D substrata (Munevar et al., 2001) and raises the interesting possibility that fibroblasts can behave as regulated-displacement machines rather than regulated-load machines (Freyman et al., 2002). Mechanics analysis may also lead to estimation of elastic energy storage and therefore the amount of work done by individual cells (Butler et al., 2002).

The observations in this study can be related to the mechanics model proposed by Munevar et al. (2001). In our 3D model, pseudopods are seen to be major components of the cellular contractile mechanism, analogous to the role played by the entire cell in their ''frontal towing'' model for cells moving on flat substrata. In that model, the cell is comprised of four zones: towing, elastic transition, cargo, and trailing end. As shown in Fig. 6, extension, compression, and shear strain appear in a pattern around the pseudopod tip, consistent with function as a towing zone. Shear ($shr[\boldsymbol{T}]$) as defined by Munevar et al. is a scalar spatial derivative of traction and thus peaks behind the towing zone where tangent load decreases sharply. In our case, an analogous transition is seen as a peak in density increment and compressive strain proximal to the pseudopod tip. Alongside pseudopods, only low shear strain is typically seen. This is consistent with a bridging function between sites of opposing tractions: one at the distal end of the pseudopod and the other at the cell body. This bridge is the equivalent of the elastic transition zone. Finally, the loads opposing the towing zone, which are seen by Munevar et al. at the trailing end, are here seen at the pseudopod-cell body boundary. Therefore, the embedded cell body can comprise both the cargo and trailing end zones.

The way traction effects propagate into a material differs markedly between rubber or PAA and collagen. Beyond mechanics in 2D versus 3D, this difference is partly due to the greater homogeneity of the synthetic materials. When cells interact with an elastic and homogeneous 2D substratum, cell-applied forces are elastically transmitted into the immediately adjacent material. Thus, the deformation due to a contracting cell diminishes uniformly with distance (as $1/r^2$). In contrast, fibroblast-driven strain in collagen does not always diminish smoothly over distance. The collagen gel is a matrix of fibers which generally respond elastically to loading. However, dense bundles of fibers radiate from cellular processes into the bulk gel, often in the direction of neighboring cells. Similar gel features have been studied by others (Tranquillo, 1999) and are thought to result from accumulated changes in ECM organization. Retraction and tensioning by many cells integrated over hours, or the more acute local effects of individual cells could cause such

changes. The resulting rigid and mechanically isolated bundles may then inelastically transmit traction over a greater range than in a uniformly elastic material.

DQA provides an opportunity to quantitatively test the hypothesis that fibroblasts within a deformable tissue construct cause mutual effects on motility and differentiation. This work quantifies how the strain field generated by an individual cell is transmitted away from that cell via the ECM. Strain patterns from individual cells extend through hundreds of microns of gel, suggesting that strain could have a role in the extensively studied mechanisms of contact guidance (Stopak and Harris, 1982; Tranquillo, 1999). In a specific example of contact guidance dubbed ''durotaxis,'' fibroblasts on elastic planar substrata respond within minutes to experimentally induced changes in substratum rigidity (Wang et al., 2001). Furthermore, it has been demonstrated directly that strain applied to single cells can cause activation of Rac, a small GTPase that regulates actin cytoskeletal function (Katsumi et al., 2002). Thus, strain fields may be allowing one cell or a group of cells to affect the behavior of distant neighbors.

As single-cell mechanics analysis becomes more common in 3D models, efforts are needed to simultaneously study signal transduction between ECM mechanics and molecular pathways regulating the cytoskeleton (Roy et al., 2002). This is especially true inasmuch as timelapse results show limited change in the distribution of GFP-α-actinin and YFP-β-actin, the major dynamic component being the rise of concentrations in pseudopod tips. One promising line of research is the use of fluorescence resonance energy transfer-based reporter assays for detecting localized activity of signaling proteins likely to play roles in adhesion and force generation (Kraynov et al., 2000; Chew et al., 2002; Katsumi et al., 2002). To the extent that such techniques require microinjection instead of reporter expression, work in 3D is more difficult than on a substratum, owing to the added difficulty of injecting cells within a matrix or shepherding cells from injection on glass through seeding into a 3D matrix. Improved bulk loading techniques (Walpita and Hay, 2002; Harkin and Hay, 1996) and reporter expression systems will help in this regard. Another approach uses only expressible chromophores and laser inactivation to experiment on cytoskeletal components within individual cells and is likely directly amenable to 3D model systems (Rajfur et al., 2002).

An online supplement to this article can be found by visiting BJ Online at http://www.biophysj.org.

We thank J. Suhan for expert work in electron microscopy; D. Pane, M. Mantarro, W. Galbraith, and S. Weinstein for microscope development; S. Saigal and D. Velegol for mechanics advice; M. Vieta and J. Lustgarten for DQA and web programming assistance; T. Brownlee and J. Airone for assistance in estimation of Poisson's ratio; and A. Marciszyn for critical reading of the manuscript.

This research was supported by National Science Foundation grants #STC MCB-8920118 and #DBI-9987393, and National Institutes of Health grant #AR-32461.

REFERENCES

Balaban, N. Q., U. S. Schwarz, D. Riveline, P. Goichberg, G. Tzur, I. Sabanay, D. Mahalu, S. Safran, A. Bershadsky, L. Addadi, and B. Geiger. 2001. Force and focal adhesion assembly: a close relationship studied using elastic micropatterned substrates. *Nat. Cell Biol.* 3:466–472.

Bell, E., B. Ivarsson, and C. Merrill. 1979. Production of a tissue-like structure by contraction of collagen lattices by human fibroblasts of different proliferative potential in vitro. *Proc. Natl. Acad. Sci. USA.* 76:1274–1278.

Brown, R. A., R. Prajapati, D. A. McGrouther, I. V. Yannas, and M. Eastwood. 1998. Tensional homeostasis in dermal fibroblasts: mechanical responses to mechanical loading in three-dimensional substrates. *J. Cell. Physiol.* 175:323–332.

Burton, K., J. H. Park, and D. L. Taylor. 1999. Keratocytes generate traction forces in two phases. *Mol. Biol. Cell.* 10:3745–3769.

Butler, J. P., I. M. Tolic-Norrelykke, B. Fabry, and J. J. Fredberg. 2002. Traction fields, moments, and strain energy that cells exert on their surroundings. *Am. J. Physiol. Cell Physiol.* 282:C595–C605.

Chew, T. L., W. A. Wolf, P. J. Gallagher, F. Matsumura, and R. L. Chisholm. 2002. A fluorescent resonant energy transfer-based biosensor reveals transient and regional myosin light chain kinase activation in lamella and cleavage furrows. *J. Cell Biol.* 156:543–553.

Cooke, M. E., T. Sakai, and D. F. Mosher. 2000. Contraction of collagen matrices mediated by $\alpha 2\beta 1$A and α(v)$\beta 3$ integrins. *J. Cell Sci.* 113: 2375–2383.

Cukierman, E., R. Pankov, D. R. Stevens, and K. M. Yamada. 2001. Taking cell-matrix adhesions to the third dimension. *Science.* 294:1708–1712.

Dickinson, R. B., J. B. McCarthy, and R. T. Tranquillo. 1993. Quantitative characterization of cell invasion in vitro: formulation and validation of a mathematical model of the collagen gel invasion assay. *Ann. Biomed. Eng.* 21:679–697.

Edlund, M., M. A. Lotano, and C. A. Otey. 2001. Dynamics of α-actinin in focal adhesions and stress fibers visualized with α-actinin-green fluorescent protein. *Cell Motil. Cytoskeleton.* 48:190–200.

Ehrlich, H. P., W. B. Rockwell, T. L. Cornwell, and J. B. Rajaratnam. 1991. Demonstration of a direct role for myosin light chain kinase in fibroblast-populated collagen lattice contraction. *J. Cell. Physiol.* 146:1–7.

Elsdale, T., and J. Bard. 1972. Collagen substrata for studies on cell behavior. *J. Cell Biol.* 54:626–637.

Farsi, J. M., and J. E. Aubin. 1984. Microfilament rearrangements during fibroblast-induced contraction of three-dimensional hydrated collagen gels. *Cell Motil.* 4:29–40.

Freyman, T. M., I. V. Yannas, Y. S. Pek, R. Yokoo, and L. J. Gibson. 2001. Micromechanics of fibroblast contraction of a collagen-GAG matrix. *Exp. Cell Res.* 269:140–153.

Freyman, T. M., I. V. Yannas, R. Yokoo, and L. J. Gibson. 2002. Fibroblast contractile force is independent of the stiffness which resists the contraction. *Exp. Cell Res.* 272:153–162.

Fung, Y. C. 1977. A first course in continuum mechanics. Prentice-Hall, Englewood Cliffs, NJ.

Grinnell, F. 1994. Fibroblasts, myofibroblasts, and wound contraction. *J. Cell Biol.* 124:401–404.

Grinnell, F. 2000. Fibroblast-collagen-matrix contraction: growth-factor signalling and mechanical loading. *Trends Cell Biol.* 10:362–365.

Grinnell, F., C. H. Ho, Y. C. Lin, and G. Skuta. 1999. Differences in the regulation of fibroblast contraction of floating versus stressed collagen matrices. *J. Biol. Chem.* 274:918–923.

Guidry, C., and F. Grinnell. 1985. Studies on the mechanism of hydrated collagen gel reorganization by human skin fibroblasts. *J. Cell Sci.* 79:67–81.

Gullberg, D., A. Tingstrom, A. C. Thuresson, L. Olsson, L. Terracio, T. K. Borg, and K. Rubin. 1990. Beta 1 integrin-mediated collagen gel contraction is stimulated by PDGF. *Exp. Cell Res.* 186:264–272.

Halliday, N. L., and J. J. Tomasek. 1995. Mechanical properties of the extracellular matrix influence fibronectin fibril assembly in vitro. *Exp. Cell Res.* 217:109–117.

Harkin, D. G., and E. D. Hay. 1996. Effects of electroporation on the tubulin cytoskeleton and directed migration of corneal fibroblasts cultured within collagen matrices. *Cell Motil. Cytoskeleton.* 35:345–357.

Harris, A. K., P. Wild, and D. Stopak. 1980. Silicone rubber substrata: a new wrinkle in the study of cell locomotion. *Science.* 208:177–179.

Hay, E. D. 1993. Extracellular matrix alters epithelial differentiation. *Curr. Opin. Cell Biol.* 5:1029–1035.

Hoffman, R. M. 1993. To do tissue culture in two or three dimensions? That is the question. *Stem Cells.* 11:105–111.

Huang, D., T. R. Chang, A. Aggarwal, R. C. Lee, and H. P. Ehrlich. 1993. Mechanisms and dynamics of mechanical strengthening in ligament-equivalent fibroblast-populated collagen matrices. *Ann. Biomed. Eng.* 21:289–305.

Katsumi, A., J. Milanini, W. B. Kiosses, M. A. del Pozo, R. Kaunas, S. Chien, K. M. Hahn, and M. A. Schwartz. 2002. Effects of cell tension on the small GTPase Rac. *J. Cell Biol.* 158:153–164.

Kolodney, M. S., and E. L. Elson. 1995. Contraction due to microtubule disruption is associated with increased phosphorylation of myosin regulatory light chain. *Proc. Natl. Acad. Sci. USA.* 92:10252–10256.

Kolodney, M. S., and R. B. Wysolmerski. 1992. Isometric contraction by fibroblasts and endothelial cells in tissue culture: a quantitative study. *J. Cell Biol.* 117:73–82.

Kraynov, V. S., C. Chamberlain, G. M. Bokoch, M. A. Schwartz, S. Slabaugh, and K. M. Hahn. 2000. Localized Rac activation dynamics visualized in living cells. *Science.* 290:333–337.

Lagerholm, B. C., S. Vanni, D. L. Taylor, and F. Lanni. 2003. Cytomechanics applications of optical sectioning microscopy. *Methods Enzymol.* 361:175–197.

Lanni, F., and T. Wilson. 2000. Grating image systems for optical sectioning fluorescence microscopy of cells, tissues, and small organisms. *In* Imaging Neurons: A Laboratory Manual. R. Yuste, F. Lanni, and A. Konnerth, editors. Cold Spring Harbor Laboratory Press, Cold Spring Harbor, New York. 8.1–8.9.

Lazarides, E., and K. Burridge. 1975. α-actinin: immunofluorescent localization of a muscle structural protein in nonmuscle cells. *Cell.* 6:289–298.

Lin, Y. C., and F. Grinnell. 1993. Decreased level of PDGF-stimulated receptor autophosphorylation by fibroblasts in mechanically relaxed collagen matrices. *J. Cell Biol.* 122:663–672.

Lo, C. M., H. B. Wang, M. Dembo, and Y. L. Wang. 2000. Cell movement is guided by the rigidity of the substrate. *Biophys. J.* 79:144–152.

Mirshahi, M., B. Azzarone, J. Soria, F. Mirshahi, and C. Soria. 1991. The role of fibroblasts in organization and degradation of a fibrin clot. *J. Lab. Clin. Med.* 117:274–281.

Munevar, S., Y. Wang, and M. Dembo. 2001. Traction force microscopy of migrating normal and H-ras transformed 3T3 fibroblasts. *Biophys. J.* 80:1744–1757.

Nakagawa, S., P. Pawelek, and F. Grinnell. 1989. Extracellular matrix organization modulates fibroblast growth and growth factor responsiveness. *Exp. Cell Res.* 182:572–582.

Oliver, T., M. Dembo, and K. Jacobson. 1995. Traction forces in locomoting cells. *Cell Motil. Cytoskeleton.* 31:225–240.

Otey, C. A., G. B. Vasquez, K. Burridge, and B. W. Erickson. 1993. Mapping of the alpha-actinin binding site within the beta 1 integrin cytoplasmic domain. *J. Biol. Chem.* 268:21193–21197.

Parizi, M., E. W. Howard, and J. J. Tomasek. 2000. Regulation of LPA-promoted myofibroblast contraction: role of Rho, myosin light chain kinase, and myosin light chain phosphatase. *Exp. Cell Res.* 254:210–220.

Pelham, R. J., Jr., and Y. L. Wang. 1999. High resolution detection of mechanical forces exerted by locomoting fibroblasts on the substrate. *Mol. Biol. Cell.* 10:935–945.

Press, W. H., S. A. Teukolsky, W. T. Vetterling, and B. P. Flannery. 1992. Numerical Recipes in C. Cambridge Unversity Press, New York, NY.

Rajfur, Z., P. Roy, C. Otey, L. Romer, and K. Jacobson. 2002. Dissecting the link between stress fibres and focal adhesions by CALI with EGFP fusion proteins. *Nat. Cell Biol.* 4:286–293.

Rosenfeldt, H., and F. Grinnell. 2000. Fibroblast quiescence and the disruption of ERK signaling in mechanically unloaded collagen matrices. *J. Biol. Chem.* 275:3088–3092.

Roskelley, C. D., P. Y. Desprez, and M. J. Bissell. 1994. Extracellular matrix-dependent tissue-specific gene expression in mammary epithelial cells requires both physical and biochemical signal transduction. *Proc. Natl. Acad. Sci. USA.* 91:12378–12382.

Roy, P., W. M. Petroll, C. J. Chuong, H. D. Cavanagh, and J. V. Jester. 1999. Effect of cell migration on the maintenance of tension on a collagen matrix. *Ann. Biomed. Eng.* 27:721–730.

Roy, P., Z. Rajfur, P. Pomorski, and K. Jacobson. 2002. Microscope-based techniques to study cell adhesion and migration. *Nat. Cell Biol.* 4:E91–E96.

Schiro, J. A., B. M. Chan, W. T. Roswit, P. D. Kassner, A. P. Pentland, M. E. Hemler, A. Z. Eisen, and T. S. Kupper. 1991. Integrin alpha 2 beta 1 (VLA-2) mediates reorganization and contraction of collagen matrices by human cells. *Cell.* 67:403–410.

Schwarz, U. S., N. Q. Balaban, D. Riveline, A. Bershadsky, B. Geiger, and S. A. Safran. 2002. Calculation of forces at focal adhesions from elastic substrate data: the effect of localized force and the need for regularization. *Biophys. J.* 83:1380–1394.

Siegel, R. C., J. C. Fu, N. Uto, K. Horiuchi, and D. Fujimoto. 1982. Collagen cross-linking: lysyl oxidase dependent synthesis of pyridinoline in vitro: confirmation that pyridinoline is derived from collagen. *Biochem. Biophys. Res. Commun.* 108:1546–1550.

Skuta, G., C. H. Ho, and F. Grinnell. 1999. Increased myosin light chain phosphorylation is not required for growth factor stimulation of collagen matrix contraction. *J. Biol. Chem.* 274:30163–30168.

Stopak, D., and A. K. Harris. 1982. Connective tissue morphogenesis by fibroblast traction. I. Tissue culture observations. *Dev. Biol.* 90:383–398.

Taylor, D. L., L. D. Harris, R. DeBiasio, S. E. Fahlman, D. L. Farkas, F. Lanni, M. Nederlof, and A. H. Gough. 1996. Automated interactive microscopy: measuring and manipulating the chemical and molecular dynamics of cells and tissues. *Proc. Soc. Photo-Optical Instr. Eng.* 2678:15–27.

Tower, T. T., and R. T. Tranquillo. 2001. Alignment maps of tissues. I. Microscopic elliptical polarimetry. *Biophys. J.* 81:2954–2963.

Tranquillo, R. T. 1999. Self-organization of tissue-equivalents: the nature and role of contact guidance. *Biochem. Soc. Symp.* 65:27–42.

Velegol, D., and F. Lanni. 2001. Cell traction forces on soft biomaterials. I. Microrheology of type I collagen gels. *Biophys. J.* 81:1786–1792.

Voytik-Harbin, S. L., B. Rajwa, and J. P. Robinson. 2001. Three-dimensional imaging of extracellular matrix and extracellular matrix-cell interactions. *Methods Cell Biol.* 63:583–597.

Walpita, D., and E. Hay. 2002. Studying actin-dependent processes in tissue culture. *Nat. Rev. Mol. Cell Biol.* 3:137–141.

Wang, H. B., M. Dembo, and Y. L. Wang. 2000. Substrate flexibility regulates growth and apoptosis of normal but not transformed cells. *Am. J. Physiol. Cell Physiol.* 279:C1345–1350.

Wang, H. B., M. Dembo, S. K. Hanks, and Y. Wang. 2001. Focal adhesion kinase is involved in mechanosensing during fibroblast migration. *Proc. Natl. Acad. Sci. USA.* 98:11295–11300.

Westergaard, H. M. 1952. Theory of Elasticity and Plasticity. Harvard University Press, Cambridge, MA.